energies

MDPI

Article

Aerothermal Performance and Soot Emissions of Reacting Flow in a Micro-Gas Turbine Combustor

Heyu Wang and Kai Hong Luo *

Mechanical Engineering Department, Faculty of Engineering Sciences, University College London, London WC1E 7JE, UK
* Correspondence: k.luo@ucl.ac.uk

Abstract: Micro-gas turbines are used for power generation and propulsion in unmanned aerial vehicles. Despite the growing demand for electric engines in a world striving for a net zero carbon footprint, combustion gas turbines will continue to play a critical role. Hence, there is a need for improved micro-gas turbines that can meet stringent environmental regulations. This paper is the first part of a comprehensive study focused on understanding the fundamental performance and emission characteristics of a micro-gas turbine model, with the aim of finding ways to enhance its operation. The study used a multidisciplinary CFD model to simulate the reacting flow in the combustion chamber and validated the results against experimental data and throughflow simulations. The present work is one of the few work that attempts to address both the aerothermal performance and emissions of the gas turbine. The findings highlight that parameters such as non-uniform outlet pressure, fuel-to-air ratio, and fuel injection velocity can greatly influence the performance and emissions of the micro-gas turbine. These parameters can affect the combustion efficiency, the formation of hot spots at the combustor–turbine interface, and the soot emissions. The results provide valuable insights for optimizing the performance and reducing the emissions of micro-gas turbines and serve as a foundation for further research into the interaction between the combustor and the turbine.

Keywords: combustor; micro-gas turbine; computational fluid dynamics

Citation: Wang, H.; Luo, K.H. Aerothermal Performance and Soot Emissions of Reacting Flow in a Micro-Gas Turbine Combustor. *Energies* **2023**, *16*, 2947. https://doi.org/10.3390/en16072947

Academic Editor: Andrzej Teodorczyk

Received: 9 February 2023
Revised: 7 March 2023
Accepted: 15 March 2023
Published: 23 March 2023

1. Introduction

Excessive consumption of fossil fuels over the past few decades has accelerated global warming. To combat this, governments and international organizations have set a goal to reach net zero emissions by 2050. Despite the growth in demand for transportation and energy, which are significant contributors to carbon emissions, technological advancements in electric-powered engines have not yet been widely adopted due to various reasons. As a result, combustion gas turbines will remain a critical component in the near future.

In the renewable energy sector, micro-gas turbines are used for electricity production. These turbines offer the advantage of being able to run on alternative fuels such as biogas, hydrogen, liquid biofuels, and so on, along with a low capital cost. The literature review by De Robbio [1] highlighted the growing role of micro-gas turbines in distributed electric and thermal energy generation from renewable sources. The review also described the integration of micro-gas turbines with other energy conversion systems such as solar fields, ORCs, and fuel cells. Banihabib and Assadi [2] recognized the potential of micro-gas turbines in the rapidly growing decentralized energy market due to their low emissions, fuel flexibility, and low maintenance. The authors discussed the challenges in improving the operational flexibility, reliability, and availability of micro-gas turbines while maintaining low environmental impact. Ji et al. [3] demonstrated the potential use of micro-gas turbines as range extenders for electric vehicles to replace diesel-based engines. Micro-gas turbines are also used as propulsors in unmanned aircraft. Capata and Saracchini [4] conducted

experiments on a miniaturized turbine for radio-controlled vehicles that run on different fuels and showed that a propane-butane mixture is more economically advantageous than kerosene. Habib et al. [5] investigated the effects of adding biofuel to Jet A and found that the addition reduced static thrust and specific fuel consumption but increased thermal efficiency. An optimum mixture reduced CO and NO pollutant emissions without a significant reduction in static thrust. Large and Pesyridis [6] explored the potential of improving the performance of existing micro turbojet gas turbine engines by converting them into turbofans.

To meet stringent environmental regulations, alternative fuels have been extensively investigated, as demonstrated by the above literature. Another aspect that has been relatively overlooked is the impact of micro-gas turbine design variables on emissions. Okafor et al. [7] experimentally examined the effects of fuel injection angle, combustor inlet temperature, equivalence ratio, and ambient pressure on flame stabilization and NOx emissions. They showed that inclined fuel injection resulted in improved flame stability and lower NH3 and NOx emissions compared with vertical injection along the combustor central axis. Zong et al. [8] proposed an external combustion air adjustment method to control the reaction zone fuel-air ratio under off-design loads. The results showed that the combustion air adjustment system reduced CO emissions but increased NOx emissions due to a longer residence time in the reaction zone. Lefebvre [9] found that the hydrogen and/or aromatics content in the fuel composition had a significant impact on flame radiation and liner wall temperature but only a slight effect on CO and NOx emissions. Chmielewski et al. [10] showed that the addition of water to the default engine fuel moderately decreased fuel consumption and significantly reduced NOx emissions. Chmielewski and Gieras [11] conducted an experimental and numerical study that showed that a variable dilution holes area design concept can increase outlet total temperature by 25% while reducing NOx and CO emissions by 40%.

Soot is a crucial pollutant emission for micro-gas turbines. These are small particles produced during hydrocarbon fuel combustion and are carcinogenic. Soot also affects the performance of gas turbines by reducing the lifespan of components due to the burning of deposited soot on the turbine surfaces. According to Naegeli et al. [12], the flame temperature significantly increases soot concentration, with a decrease in the H/C ratio leading to an even stronger increase in soot concentration. Rault et al. [13] observed an increase in soot formation in 10% ethanol blend flames compared with original Jet A-1 flames in their experiments, which was attributed to changes in the flame structure.

Micro-gas turbines have several major components besides the combustor, including a compressor and a turbine. Interactions between these components can impact the performance and emission characteristics of the turbine. In previous work by the authors [14], the effects of diffuser design and compressor outlet flow on the aerodynamic performance of the combustor were studied. Results showed that the diffuser–combustor integrated design, developed with the compressor outlet flow taken into account, had potential for improved performance. In real-life operation, micro-gas turbines face numerous sources of uncertainty, such as variations in boundary layer thickness, manufacturing variations in blade rows [15–20], and more. These uncertainties, combined with interactions between components, can significantly impact performance. For instance, the combustor outlet flow results in a non-uniform inlet flow to the turbine stages [21,22], and the combustor hot streak can degrade the aerothermal performance of the turbine [23–25]. The current work is the first part of a more comprehensive project aimed at understanding the fundamental aerothermal performance and emission characteristics of a micro-gas turbine model and finding ways to improve its operation. The study includes simulating a reacting combustor flow in conjunction with aerodynamic simulation of other gas path components. This present work focuses on the combustor with a reacting flow, investigating the effects of aerodynamic boundary conditions and fuel injection parameters in detail.

2. Numerical Methods

The solver ANSYS CFX is adopted in the current work. It is an implicit finite-volume-based Navier–Stokes solver. The governing equations that represent the conservation of mass, momentum, and energy at each instantaneous time step are described as follows:

$$\begin{gathered} \frac{\partial \rho}{\partial t} + \nabla \cdot (\rho \boldsymbol{U}) = 0, \\ \frac{\partial (\rho \boldsymbol{U})}{\partial t} + \nabla \cdot (\rho \boldsymbol{U} \otimes \boldsymbol{U}) = -\nabla p + \nabla \cdot \tau, \\ \frac{\partial (\rho \boldsymbol{H})}{\partial t} - \frac{\partial p}{\partial t} + \nabla \cdot (\rho \boldsymbol{U} \boldsymbol{H}) = -\nabla \cdot (\lambda \nabla T) + \nabla \cdot (\boldsymbol{U} \cdot \tau) \end{gathered} \tag{1}$$

The advection terms are discretized by the bounded high-resolution scheme similar to Barth and Jespersen [26]. Pressure-velocity coupling is performed by the 4th order smoothing algorithm similar to Rhie and Chow [27]. The algebraic multigrid method is used to accelerate the solver convergence rate. The solution is marched with the pseudo time step until the convergence criteria are reached and the residuals drop several orders of magnitude. To close the governing equations, the $k - \omega$ SST turbulence model [28] is adopted.

2.1. Combustion Modeling

In this section, the combustion model for the reacting mixture in the combustor is presented. In the present study, the fuel type for the micro-gas turbine is Jet-A fuel ($C_{12}H_{23}$). This is the most common fuel for micro-gas turbine applications, although bio-fuels and hydrogen have been increasingly used to achieve greener emissions and fuel flexibility. The transport equations for the combustion mode use the same algorithms for multiphase flow with additional source terms due to chemical reactions:

$$\frac{\partial (\rho Y_I)}{\partial t} + \nabla \cdot (\rho \boldsymbol{U} Y_I) = \nabla \left(\Gamma_{I_{eff}} (\nabla Y_I) \right) + S_I \tag{2}$$

where Y_I is the component mass fraction; and S_I is the component chemical reaction rate.

The eddy dissipation model is adopted in this study due to its computational efficiency and robustness. It is suitable for large-scale industrial simulations as in this project, where the whole micro-gas turbine needs to be simulated at various operating conditions. The eddy dissipation model is built upon the concept that chemical reaction is fast relative to the flow transport process. The model assumes that the reaction rate is proportional to the reactants mixing time, which is also proportional to the ratio of turbulent dissipation and turbulent kinetic energy:

$$\text{reaction rate} \propto \frac{\varepsilon}{k} \tag{3}$$

where k is the turbulent kinetic energy; ε is the rate of dissipation of turbulent kinetic energy.

The two-step chemical kinetic mechanism of the Jet-A fuel adopted in the present work is shown below. A reduced kinetic mechanism is used to balance the cost/time of simulation against the prediction accuracy. Despite being relatively simple compared with the full kinetic mechanisms (which are also subject to several modeling uncertainties), reduced kinetic mechanisms have been shown to reproduce reasonably the key quantities of interest including heat release rates, flame temperature, and species concentration. For example, one can refer to References [29–32] for previous works that adopted reduced kinetic mechanisms for Jet-A and other fuels.

$$C_{12}H_{23} + 11.75O_2 \rightarrow 12CO + 11.5H_2O \tag{4}$$

$$CO + 0.5O_2 \rightarrow CO_2 \tag{5}$$

The reaction rate is calculated based on the modified Arrhenius equation:

$$k = AT^n \exp(-E/RT) \tag{6}$$

where A is the pre-exponential collision frequency factor; T is the temperature; n is the temperature exponent; E is the activation energy; and R is the universal gas constant.

2.2. Droplet Breakup Modeling

Liquid Jet-A fuel is pumped via the fuel feed into the combustor. In the micro-gas turbine model adopted in this study, liquid Jet-A fuel is vaporized to gaseous Jet-A fuel. The vaporization process is simulated by the droplet breakup modeling approach. There are a few droplet breakup models to choose from in the solver ANSYS CFX. In this section, they are briefly described and one of the models are chosen in a further study.

Firstly, the Taylor Analogy Breakup (TAB) model [33] is discussed. It is built upon the Taylor analogy, in which the droplet distortion can be described as a one-dimensional spring-mass system. The TAB model assumes that the droplet velocity acts as a damping force and the surface tension acts as a restoring force. If the deviation of the particle equator from its equilibrium position has become larger than half the droplet radius, breakup deems to occur. The Sauter mean radius of the child droplets after breakup is determined based on the energy balance between the parent and child droplets:

$$\frac{r_{p,\text{parent}}}{r_{p,\text{child}}} = 1 + 0.4K + \frac{\rho_p r_{p,\text{parent}}^3}{\sigma} \dot{y}_0{}^2 \left(\frac{6K - 5}{120} \right) \tag{7}$$

where $K = 10/3$ is the energy ratio factor; and $\dot{y}_0$ is the initial value of the distortion rate of change and assumed to be zero.

An improved version of the TAB model is the Enhanced Taylor Analogy Breakup (ETAB) model introduced by Tanner [34]. This model uses the same droplet distortion mechanism as the standard TAB model, but with a different relation for the description of the breakup process. In the ETAB model, the rate of child droplet generation is assumed to be proportional to the number of child droplets:

$$\frac{r_{p,\text{child}}}{r_{p,\text{parent}}} = e^{-K_{br} t} \tag{8}$$

where K_{br} is dependent on the breakup regime and Weber number.

Besides the TAB and ETAB models, there are several other droplet breakup models such as the Cascade Atomization and Breakup (CAB) [35], the Reitz and Diwakar model [36], etc. Wahba and Nawar [37] compared predictions of several droplet breakup models for validation against experiments by Sedarsky et al. [38] and Liu et al. [39] as well as their own studies in a gas turbine system. In their study, the ETAB model consistently showed the least deviation from experimental measurements. Therefore, the ETAB model is chosen in this study.

2.3. Soot Modeling

Besides the aerothermal performance of the micro-gas turbine, its emission characteristics are of interest. In this section, modeling of soot formation is described. The Magnussen soot model [40] is adopted. In this model, soot is assumed to form from a gaseous fuel in two stages: the formation of radical nuclei and the formation of soot particles from these nuclei. Extra transport equations need to be solved for soot modeling:

$$\begin{aligned} \frac{\partial(\overline{\rho}\widetilde{X_N})}{\partial t} + \nabla \cdot \left(\overline{\rho} \boldsymbol{u} \widetilde{X_N} \right) &= \nabla \widetilde{X_N} \left(\overline{\mu} + \frac{\mu_t}{Pr_t} \right) + \widetilde{S}_{\text{nuclei},f} + \widetilde{S}_{\text{nuclei},c} \\ \frac{\partial(\overline{\rho}\widetilde{Y_S})}{\partial t} + \nabla \cdot \left(\overline{\rho} \boldsymbol{u} \widetilde{Y_S} \right) &= \nabla \widetilde{Y_S} \left(\overline{\mu} + \frac{\mu_t}{Pr_t} \right) + \widetilde{S}_{\text{soot},f} + \widetilde{S}_{\text{soot},c} \end{aligned} \tag{9}$$

where X_N is the specific concentration of radical nuclei; and Y_S is the soot mass fraction.

The modeling procedures comprise of three independent parts:

- Formation of nuclei and soot particles according to Tesner et al. model [41];
- Combustion of nuclei and soot particles;

- Magnussen's Eddy Dissipation Concept for modeling the effect of turbulence on mean reaction rates.

2.4. Data Post-Processing

There are various aerothermal quantities of interest in the current work that are not readily available from the raw simulation. Additional calculations need to be performed to post-process these data. The first variable of interest is the combustion efficiency η_{cc}:

$$T_{04} = T_{03} + \frac{\eta_{cc} f HV}{c_{pg}} \tag{10}$$

where η_{cc} is the combustion efficiency; f is the fuel-to-air ratio; $HV = 43.1$ MJ/kg is the Jet-A fuel heating value; and c_{pg} is the gas specific heat.

For the validation purposes, the engine thrust F is of interest. It can be calculated as the momentum change across the engine, assuming the pressure at the nozzle exit is equal to the freestream pressure:

$$F = \dot{m}_e V_e - \dot{m}_0 V_0 \tag{11}$$

where $\dot{m}_e$ is the exit mass flow rate; $\dot{m}_0$ is the inlet mass flow rate; V_e is the exit gas velocity; and V_0 is the inlet gas velocity.

3. Test Case Descriptions

3.1. Geometry

The micro-gas turbine adopted in the current work is of turbojet type. It is built upon the KJ66 micro-gas turbine model [42]. Its typical use is for small radio-controlled unmanned aerial vehicles. This model and its modified variant [43–45] have been investigated extensively by other researchers due to the availability of its geometrical and operational information. Figure 1a shows the cross-section and Figure 1b shows the whole view of the three-dimensional CAD model of the micro-gas turbine. As can be seen, this micro-gas turbine model comprises of a single-stage centrifugal compressor, an annular combustion chamber, a single-stage axial turbine, and an exhaust. The combustion chamber, which is the focus in the current work, is a reverse-flow type. It has several vaporizing tubes inside the chamber. The fuel feed supply pipes are not modeled for simplicity, and the liquid fuel is injected inside the vaporizing tubes. The droplet breakup models then convert the liquid fuel into the gaseous fuel by the vaporization process.

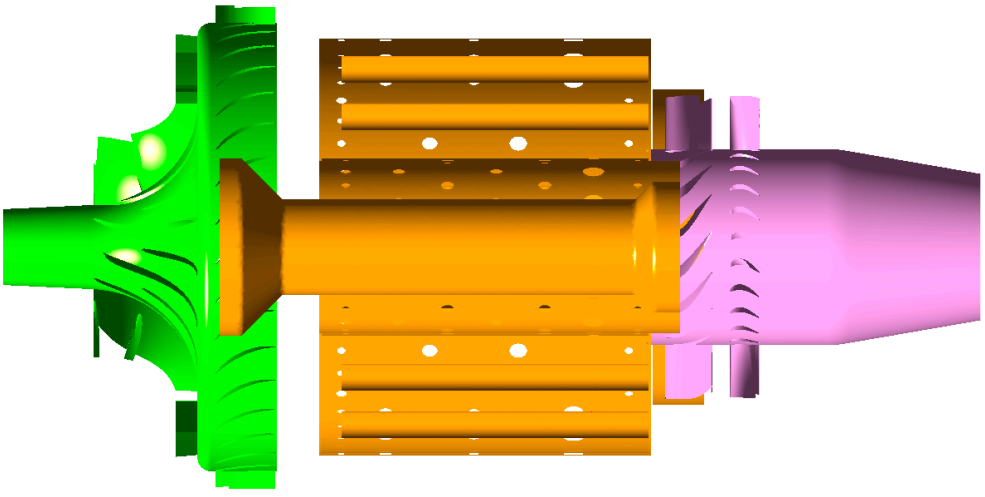

(**a**)

Figure 1. *Cont.*

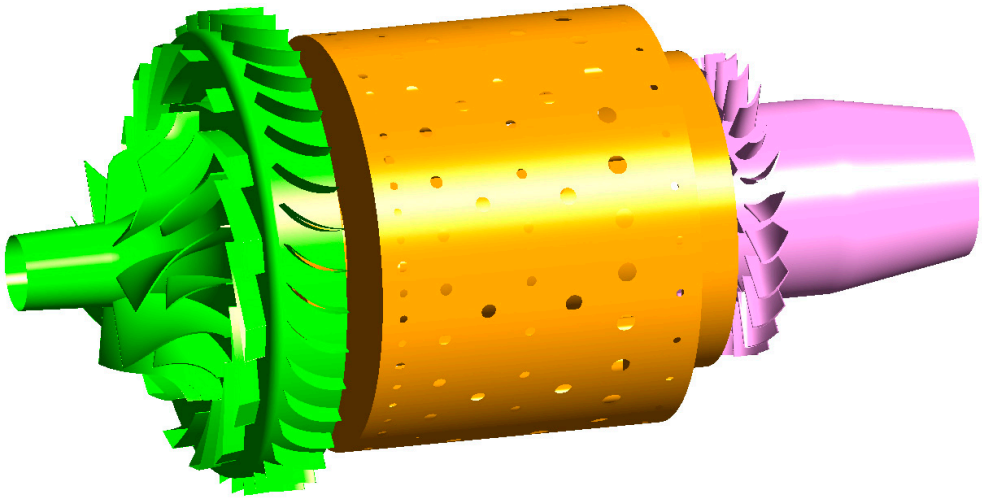

(**b**)

Figure 1. Three-dimensional CAD model of the micro-gas turbine: (**a**) cross-section view; (**b**) whole view.

3.2. Computational Domain and Mesh

Only the combustion chamber is investigated in the current work. Figure 2 shows the computational domain and mesh of the combustion chamber. The computational domain lies between the compressor outlet/combustor inlet interface and the turbine inlet/combustor outlet interface. Only a single sector is modeled in the current work to reduce the computational cost. With a closer look at Figure 2, the outer and inner walls of the combustion chamber can be visualized clearly. On the inner walls of the combustion chamber, there are several dilution holes of varying sizes and locations. These holes provide air supply to complement the fuel combustion as well as cooling the combustion chamber walls. The combustion chamber geometry is meshed using the software ICEM. The surface meshes are quad-dominant and the volume meshes are hexa-dominant to ensure the high quality.

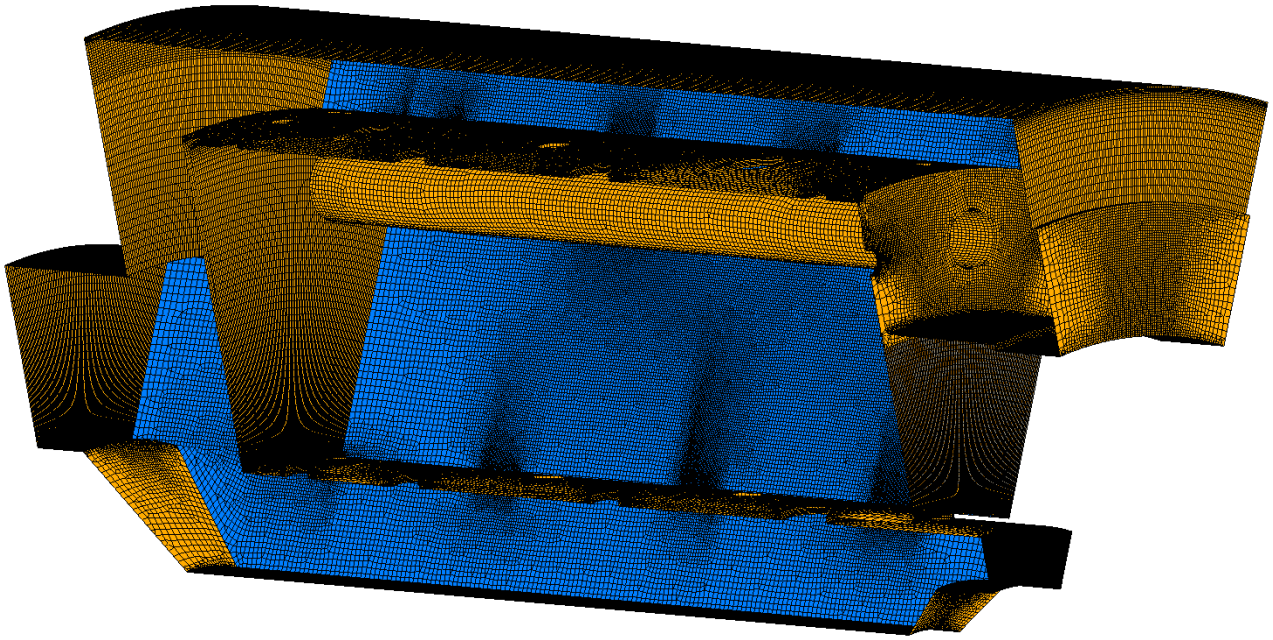

(**a**)

Figure 2. *Cont.*

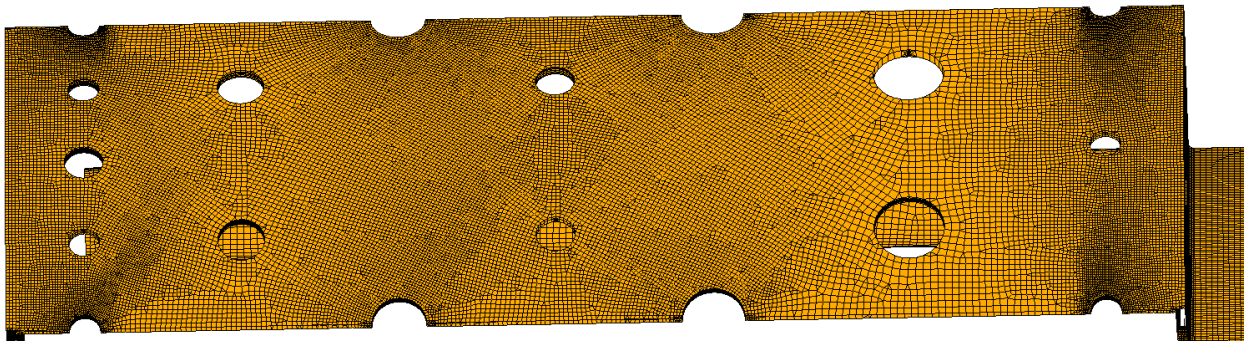

(**b**)

Figure 2. Computational domain and mesh of the combustion chamber sector: (**a**) side view; (**b**) top view.

3.3. Simulation Setup and Boundary Conditions

A single-sector computational model of the combustion is used, with the two outermost interfaces set with rotational periodicity. At the combustor inlet, total pressure, total temperature, and flow angles are specified. At the combustor outlet, the static pressure is specified. These boundary conditions are uniform in the baseline case, aligned with the average values obtained from a whole engine simulation at the maximum thrust operating conditions. Liquid Jet-A fuel is injected inside the vaporizing tube at a specified mass flow rate, with specified injection angle and velocity. All wall surfaces are modeled as adiabatic no-slip surfaces.

3.4. Mesh Sensitivity Study

A mesh sensitivity study is crucial to ensure that the numerical results are not dependent on the mesh size. In this study, the mesh size is gradually refined until the quantities of interest change slightly. Figure 3 presents the results of the mesh sensitivity study. The two quantities of interest are combustion efficiency (Figure 3a) and soot concentration at the combustor outlet (Figure 3b). The results indicate that the numerical predictions converge for configurations with more than 3 million mesh elements. Configurations with a mesh count lower than 3 million exhibit a significant deviation from the results obtained using a fine mesh.

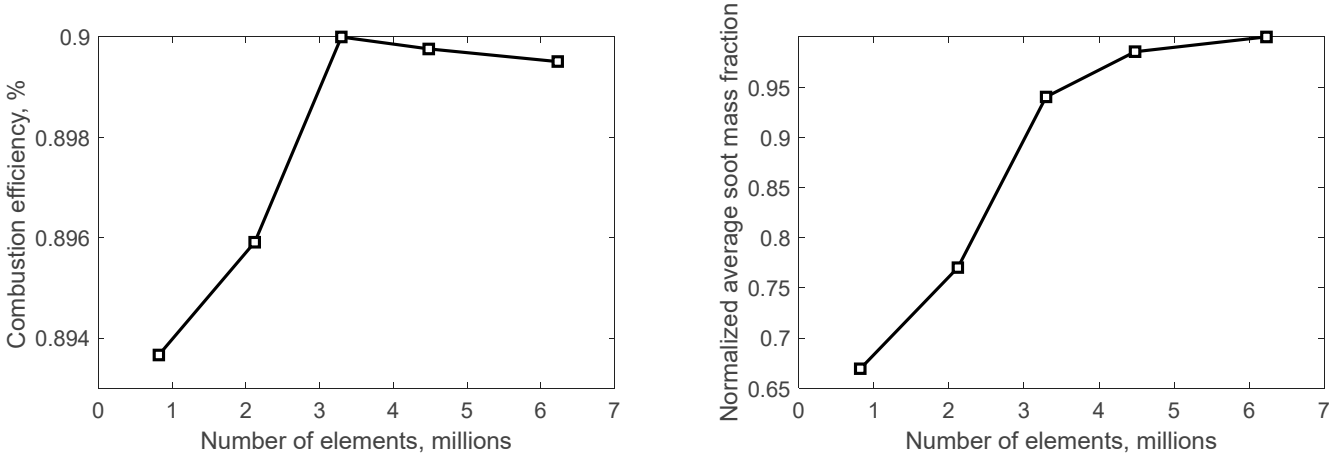

(**a**) (**b**)

Figure 3. Results of mesh sensitivity study: (**a**) combustion efficiency; (**b**) normalized soot mass fraction.

Both combustion efficiency and soot formation are sensitive to the temperature distribution at the outlet. In the next steps, the total temperature distribution at the combustor outlet is further examined. Figure 4 shows the total temperature contours at the combustor outlet for different mesh size configurations. Firstly, a hot spot is evident, characterized by a high temperature zone at mid-span. As seen, the spatial extent and temperature level of the hot spot reduce with mesh refinement. The configurations shown in Figure 4c–e are qualitatively similar, reinforcing the previous observation regarding combustion efficiency. As a result, the mesh with 4.5 million elements for a single sector is chosen as the final mesh for the current study considering the balance of accuracy and computational cost.

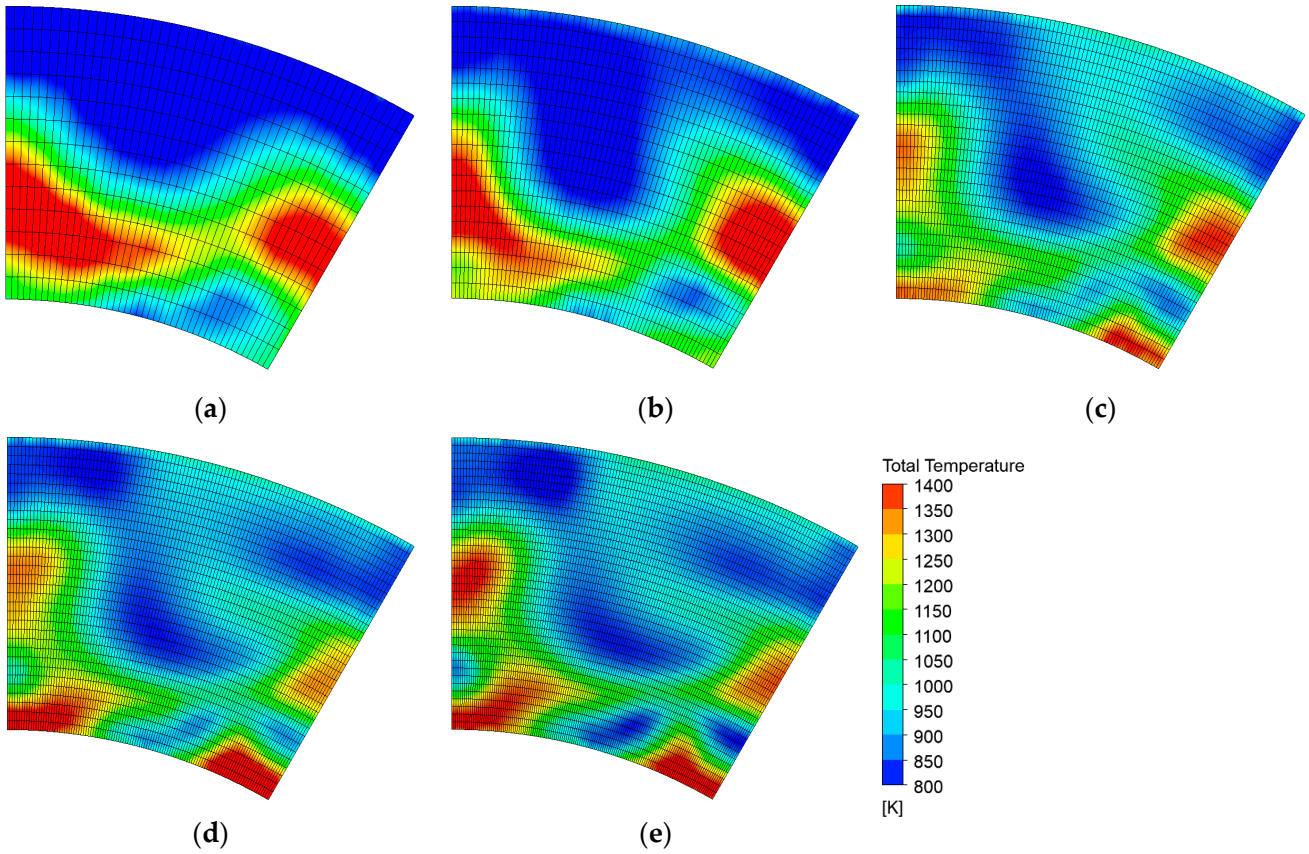

Figure 4. Combustor outlet total temperature contour of different mesh size configuration: (**a**) 0.8 M; (**b**) 2.1 M; (**c**) 3.3 M; (**d**) 4.5 M; (**e**) 6.2 M.

3.5. Validations

In this section, the simulation method is validated using data from the public domain, including experiments by Schreckling [42] and numerical throughflow simulations by Yang et al. [44]. Two parameters, engine thrust and exhaust temperature, are compared. Figure 5 displays the validation results for engine thrust and exhaust temperature. The chosen operating point in the current work, at maximum thrust around 120,000 rpm, is slightly under-predicted for thrust and slightly over-predicted for exhaust temperature, but both are close to the expected results. A detailed analysis of the whole engine model is not the focus of this study and is presented in a separate report. The validation results confirm the validity of the CFD simulation approach used in this study. Further validations for the turbomachinery gas path for popular test geometries have been carried out using the same code and simulation method. However, they are not shown in the present work and will be released in future works that involved turbomachinery components.

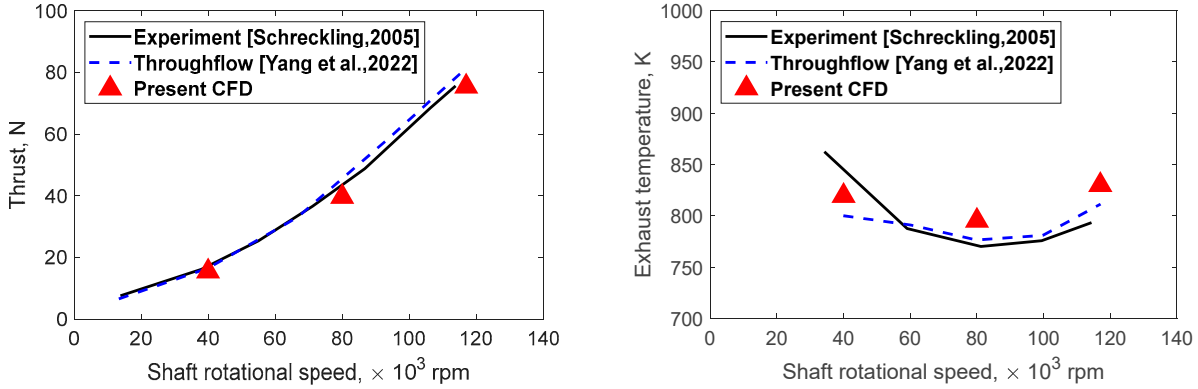

Figure 5. Full engine validation results against the experiment of Schreckling [42] and throughflow simulations of Yang et al. [44] for: (**a**) engine thrust; (**b**) exhaust temperature.

4. Results and Discussion

In this section, the main results of the current work is discussed. Firstly, the baseline configuration is analyzed to understand the fundamental flow mechanism within the micro-gas turbine combustor. Then, sensitivity studies of the outlet boundary conditions and fuel injection parameters are conducted. This study investigates the aerothermal performance and soot emission characteristics of the micro-gas turbine combustor under different design and operating conditions.

4.1. Baseline Configuration

Figure 6 shows the streamwise velocity contour at the cross-sectional surface of the combustion chamber with streamlines overlaid to aid visualization of the flow field. The streamwise velocity is high at both the inlet (compressor–combustor interface) and outlet (combustor–turbine interface). The flow field after passing the inlet is divided into two main paths. The first path follows the streamwise direction to the rear of the combustion chamber along the upper part of the chamber and then goes through the vaporization tube to mix with the fuel, demonstrating the reverse-flow combustor concept. The second flow path goes downward and then follows the streamwise direction along the lower part of the chamber. Part of the flow goes through the dilution holes as it travels in the streamwise direction. The combustion chamber has unique dump corners, characterized by low velocity and swirling flow zones, which retard the incoming flow from the compressor to a velocity suitable for combustion and maintaining the flame. As a result, it can be seen that the flow inside the chamber core has low velocity and high swirling flow, promoting efficient fuel mixing and combustion.

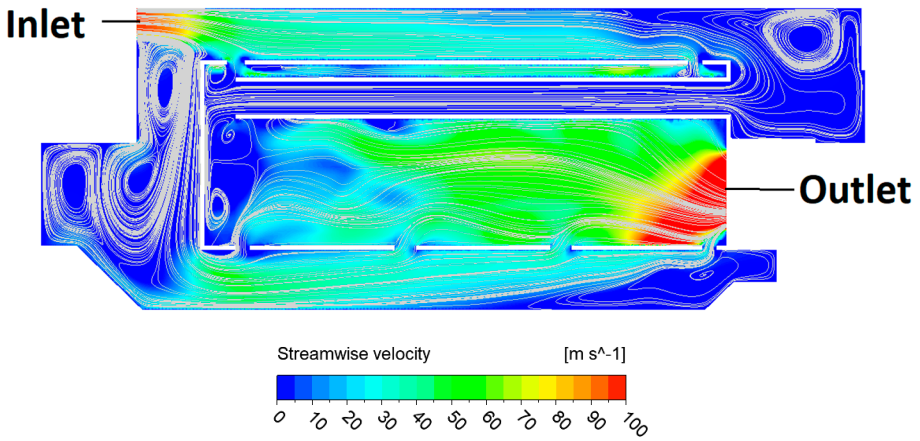

Figure 6. Streamwise velocity contour at the combustion chamber cross-section surface.

Figure 7 shows the streamwise temperature contour at the cross-section surface of the combustion chamber. The flame can reach up to 2400–2600 Kelvin degrees at the chamber core. It is interesting to note that the flame has the tendency to move downward, which would interact with the lower inner combustor casing. Thus, this part of the combustion chamber is prone to overheating if the cooling system is not designed properly.

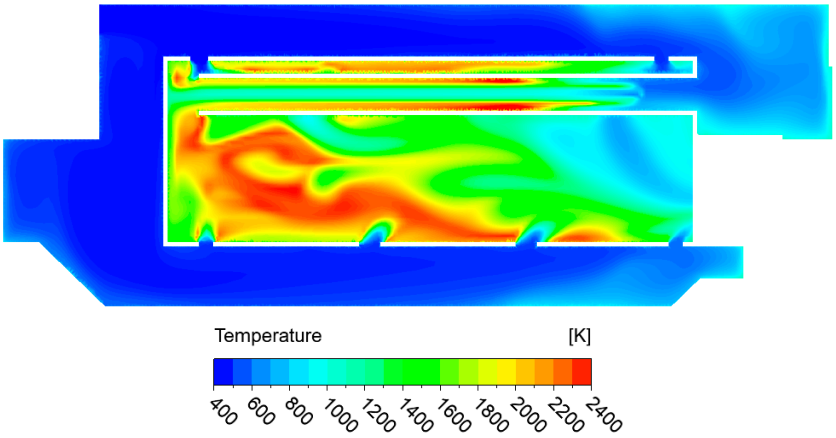

Figure 7. Streamwise temperature contour at the combustion chamber cross-section surface.

Figure 8a,b show the total temperature and the soot concentration at the combustor outlet, respectively. A hot-spot can be seen at mid-span (Figure 8a), which is responsible for the hot streak that travels downstream to the turbine stage and reduces the nozzle guide vane's lifetime. In this micro-gas turbine model, there is also an end-wall hot-spot. Like the mid-span hot spot, it can overheat the turbine hub casing, reducing the performance and lifetime of the micro-gas turbine system. The soot concentration contour (Figure 8b) has a similar spatial distribution compared with the total temperature contour (Figure 8a), confirming that soot formation is highly correlated with the local temperature field.

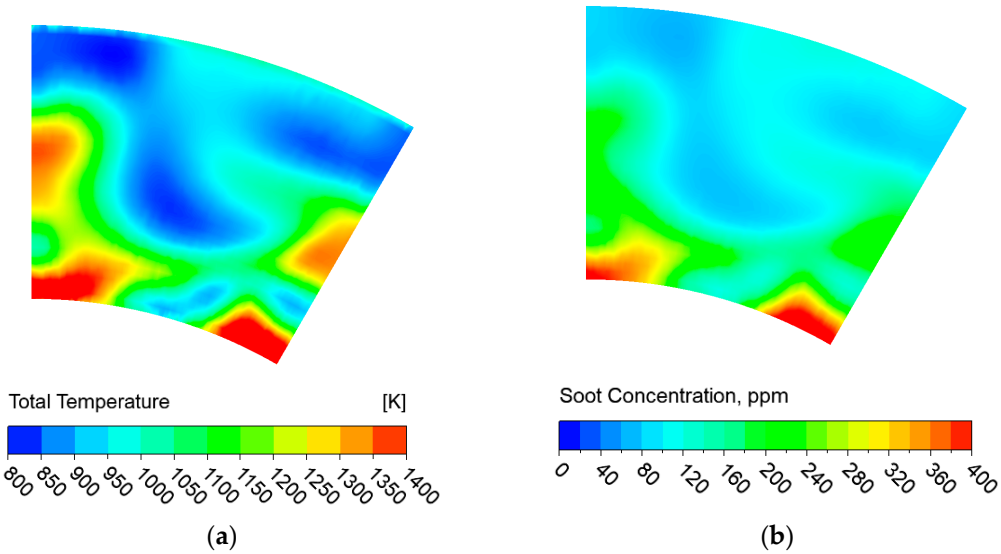

Figure 8. Combustor outlet contours: (**a**) total temperature; (**b**) soot concentration.

4.2. Effects of Outlet Flow Non-Uniformity

In this section, the impact of outlet boundary conditions on the micro-gas turbine combustor is analyzed. The baseline configuration uses a uniform outlet static pressure boundary condition, which corresponds to the average value obtained from the whole engine model analysis. However, the presence of downstream nozzle guide vanes (NGVs) creates a pressure field upstream that affects the combustor simulation domain. Figure 9

displays the pressure contour at the combustor–turbine interface in the fully coupled simulation model, showing an increase in pressure in certain circumferential and radial locations corresponding to the potential field of the turbine vanes. The results from the baseline configuration with uniform outlet pressure are compared with those obtained from the simulation with the non-uniform outlet pressure boundary condition.

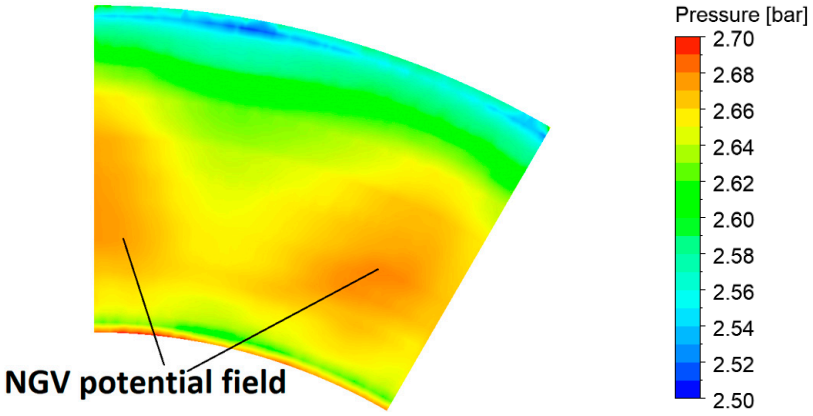

Figure 9. Non-uniform pressure distribution at the combustor–turbine interface.

Figure 10 shows the contour of the total temperature at the combustor outlet under uniform (Figure 10a) and non-uniform (Figure 10b) outlet pressure boundary conditions. Both simulations exhibit similar spatial distributions, featuring mid-span and end-wall hot-spots. However, the non-uniform outlet simulation predicts a higher temperature at the combustor outlet, reflecting the zones with increased static pressure as seen in Figure 9. This aligns with the ideal gas law, which states that pressure levels are proportional to temperature.

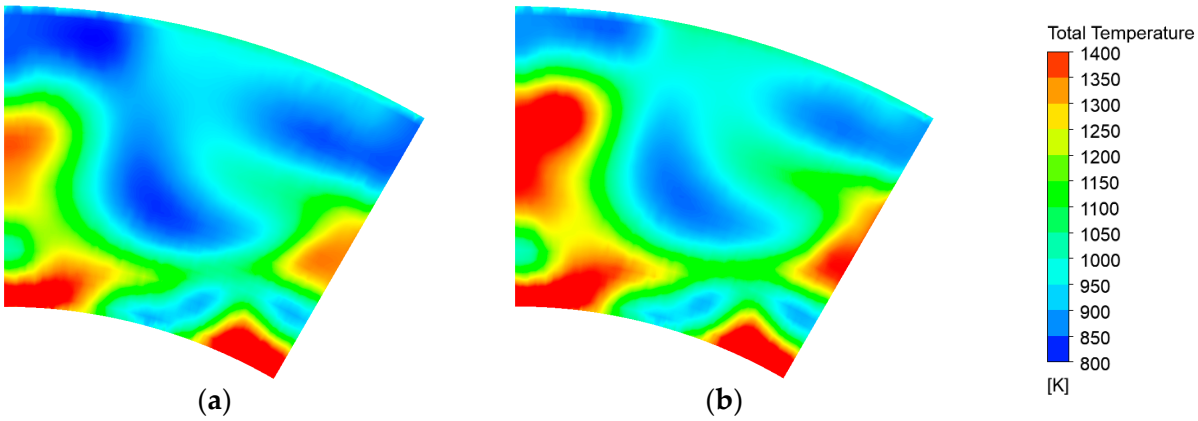

Figure 10. Combustor outlet total temperature contour with: (**a**) uniform outlet; (**b**) non-uniform outlet pressure boundary condition.

Figure 11 compares the circumferential distribution of the total temperature at the mid-span of the combustor outlet. The overall shape of the total temperature remains similar in the circumferential direction, which supports the previous observation shown in Figure 10. The total temperature levels in the non-uniform outlet case are generally higher than in the uniform case. Notably, the circumferential location of the trough shifts from around 0.6 in the uniform case to around 0.5 in the non-uniform case. Although not discussed in detail in this paper, the circumferential location of the hot spot has a significant impact on the heat transfer in the downstream turbine stage.

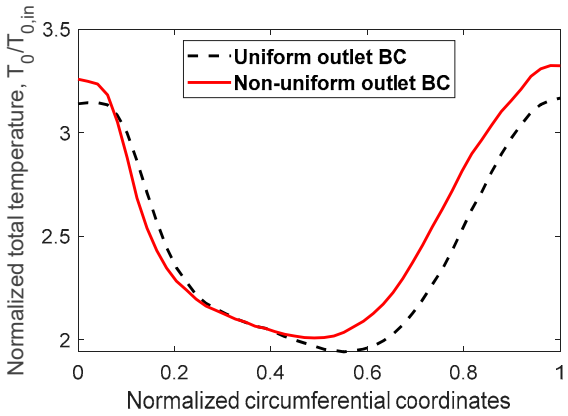

Figure 11. Total temperature circumferential distribution at the combustor outlet mid-span.

Figure 12 shows the contour of the soot concentration at the combustor outlet under uniform (Figure 12a) and non-uniform (Figure 12b) outlet pressure boundary conditions. The general spatial distribution is similar among the two simulations. The soot concentration (Figure 12) is highly correlated to the total temperature shown in Figure 11.

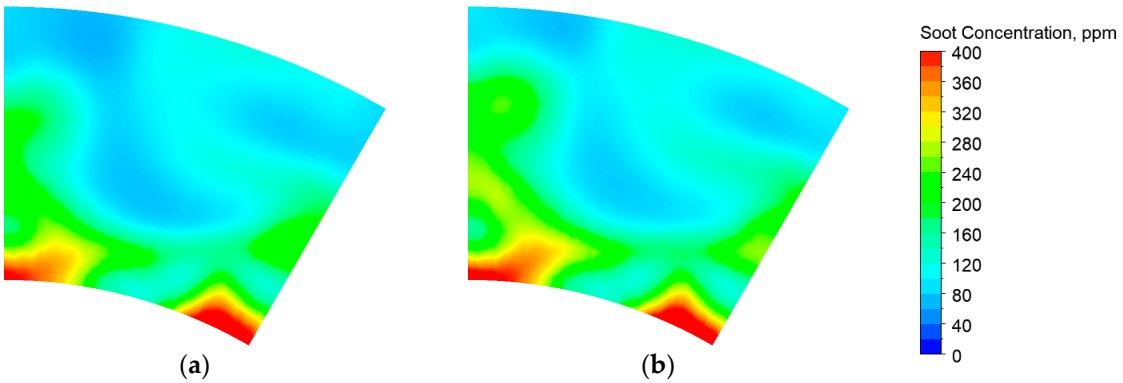

Figure 12. Combustor outlet soot concentration contour with: (**a**) uniform outlet; (**b**) non-uniform outlet pressure boundary condition.

Figure 13 compares the circumferential distribution of the soot concentration at the mid-span of the combustor outlet. The soot concentration levels in the non-uniform outlet case are slightly higher than in the uniform case. Notably, the circumferential location of the trough shifts from around 0.6 in the uniform case to around 0.5 in the non-uniform case. Figure 13 shows a better qualitative comparison that is difficult to clearly observe in Figure 12.

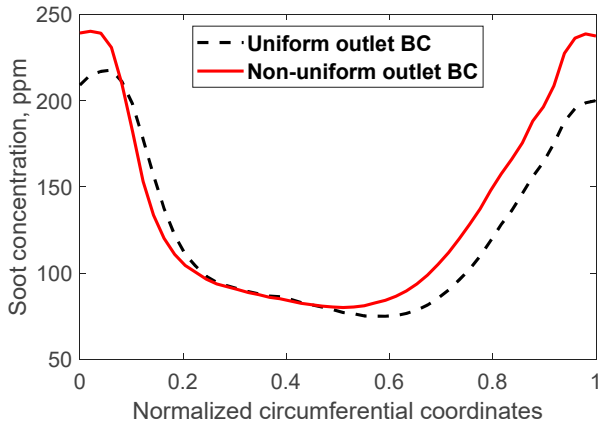

Figure 13. Soot concentration circumferential distribution at the combustor outlet mid-span.

Table 1 compares the combustor efficiency and the average soot concentration of the two simulations with uniform and non-uniform outlet pressure boundary condition. It can be seen that the uniform case has a slightly higher combustor efficiency while having about 9% lower soot concentration at outlet. Therefore, it can be concluded that the uniform outlet pressure boundary condition overestimates the combustion efficiency, while underestimating the soot concentration. This finding suggests that a fully coupled combustor–turbine is highly desired for a better prediction of performance and emission characteristics. If the individual component is to be simulated in a separate manner due to the simulation time and cost prohibitive requirements, exchange of the boundary conditions need to be performed for at least a few iterations.

Table 1. Comparison between uniform outlet BC and non-uniform outlet BC.

	Uniform Outlet BC	Non-Uniform Outlet BC
Combustor efficiency	0.9002	0.8928
Average soot concentration	134.283 ppm	146.426 ppm

4.3. Effects of Fuel-to-Air Ratio

In this section, the effects of fuel-to-air ratio is analyzed in more details. It is defined as the ratio of the Jet-A fuel mass flow rate to the engine air mass flow rate:

$$FAR = \dot{m}_{fuel} / \dot{m}_{air} \tag{12}$$

where FAR is the fuel-to-air ratio; $\dot{m}_{fuel}$ is the fuel mass flow rate; and $\dot{m}_{air}$ is the engine air mass flow rate.

In fact, the fuel-to-air ratio is not an explicit control parameter. Depending on the operating point of the engine, a specific fuel mass flow rate is consumed corresponding to a given shaft rotational speed. Thus, the fuel mass flow rate is typically an unknown, and is calculated iteratively to match the compressor power and the turbine power for a given shaft rotational speed. As is common practice, for example, in Briones at el. [46], the fuel mass flow rate was calculated using the secant root-finding method:

$$\dot{m}_{fuel,n+1} = \dot{m}_{fuel,n} + \left(\dot{W}_{c,n} - \dot{W}_{t,n}\right) \times \frac{\dot{m}_{fuel,n} - \dot{m}_{fuel,n-1}}{\left(\dot{W}_{c,n} - \dot{W}_{t,n}\right) - \left(\dot{W}_{c,n-1} - \dot{W}_{t,n-1}\right)} \tag{13}$$

where $\dot{W}_c$ is the compressor power; $\dot{W}_t$ is the compressor power; and n is the time step n^{th}.

A similar iterative approach was also adopted in Yang et al. [40]:

$$\dot{m}_{fuel,n+1} = \frac{-1 - RP_{n-1}}{RP_n - RP_{n-1}} \times \left(\dot{m}_{fuel,n} - \dot{m}_{fuel,n-1}\right) + \dot{m}_{fuel,n-1} \tag{14}$$

where RP is the ratio of turbine power to the compressor power; and n is the time step n^{th}.

Therefore, the investigation of the fuel-to-air ratio in this section can also be regarded as the investigation of the micro-gas turbine's performance at different working conditions along the operating line. Figure 14 shows the effect of fuel-to-air ratio on the combustion efficiency. The trend is clearly linear with an increase in the combustion efficiency when the fuel-to-air ratio decreases.

Because the combustion efficiency is strongly related to the total temperature values, we next analyze the total temperature distribution pattern. Figure 15 shows the circumferential distribution of the total temperature at the mid-span of the combustor outlet for different fuel-to-air ratios, which characterize the mid-span hot-spot. Changes in the fuel-to-air ratio significantly affect not only the level of the outlet temperature but also its pattern. As the fuel-to-air ratio decreases, both the peak and trough temperature decrease, indicating a reduction in the severity of the hot-spot at the combustor–turbine interface.

Notably, the relative circumferential location of the peak and trough total temperature also change. It should be noted that the combustor and nozzle guide vane circumferential locations remain fixed for all investigations.

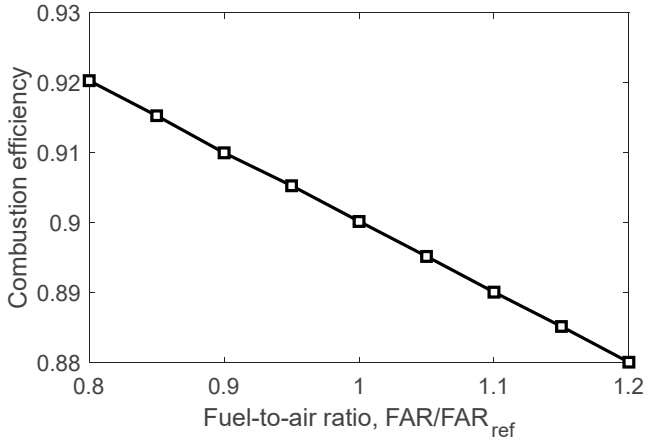

Figure 14. Effect of the fuel-to-air ratio on the combustion efficiency.

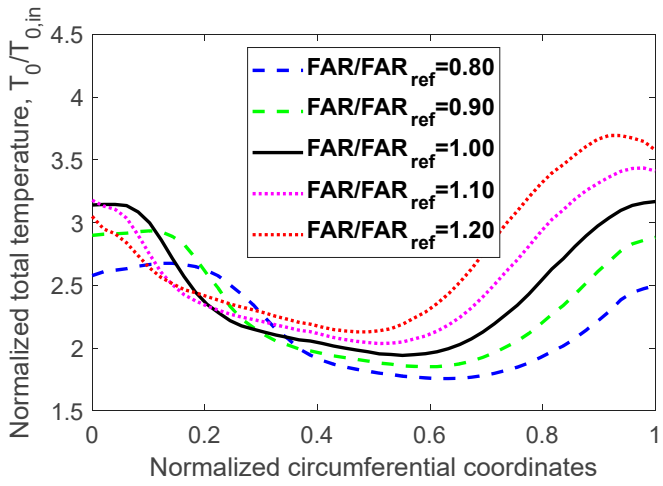

Figure 15. Total temperature circumferential distribution at the combustor outlet mid-span for different values of fuel-to-air ratio.

Figure 16 shows the average soot concentration at the combustor outlet for different values of fuel-to-air ratio. This time a non-monotonic relationship is observed. The optimum value of fuel-to-air ratio in terms of soot emissions is around 1.05, slightly larger than the baseline value in the current study. For fuel-to-air ratio values smaller or larger than this optimum value, the amount of soot emissions increase. Decreasing the fuel-to-air ratio tends to have a higher rate of soot formation.

4.4. Effects of Fuel Injection Velocity

Fuel injection velocity is another control parameter to be considered. In reality, fuel injection velocity can be realized by modifications of the fuel injector geometry (for example those in Ref [47]). However, due to the simplification of spray modeling adopted in the present work, parametric changes in fuel injection velocity can be calculated directly. Figure 17 shows the effect of fuel injection velocity on combustion efficiency. The trend line remains almost constant with no significant change when fuel injection velocity is modified, indicating that fuel injection velocity has no impact on combustion efficiency.

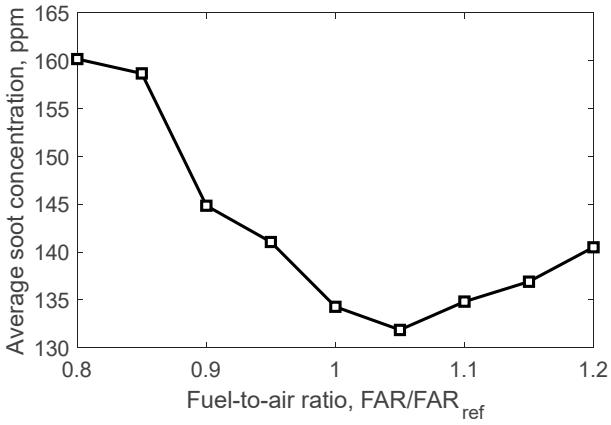

Figure 16. Effect of the fuel-to-air ratio on the soot concentration.

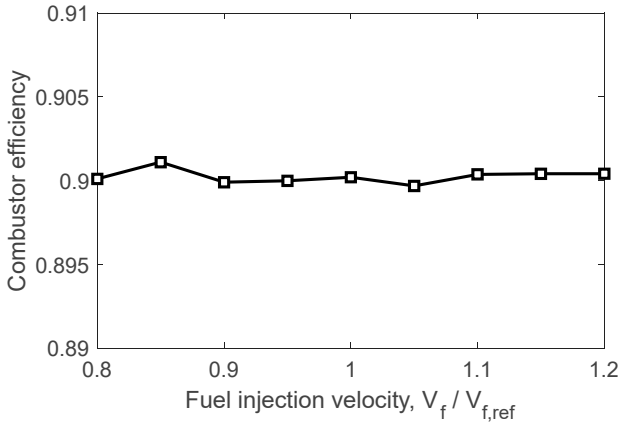

Figure 17. Effect of the fuel injection velocity on the combustion efficiency.

Similarly to the previous study, the total temperature distribution at the outlet is analyzed. Figure 18 shows the total temperature distribution in the circumferential direction at the combustor outlet mid-span for different values of fuel injection velocity. No significant change in temperature can be observed with different fuel injection velocities. The curves almost lay on top of each other. This confirms the observation form the combustion efficiency calculation (Figure 17), that is, the fuel injection velocity has no significant impact on the combustion efficiency.

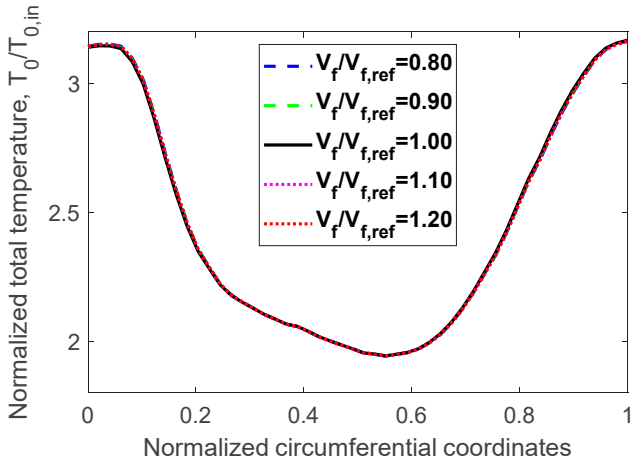

Figure 18. Total temperature circumferential distribution at the combustor outlet mid-span for different values of fuel injection velocity.

Figure 19 shows the average soot concentration for different values of fuel injection velocity. Although a non-linear pattern is observed, the trend is monotonic. As the fuel injection velocity decreases, the average soot concentration consistently increases. However, the rate of increasing is highest near the baseline value. Further away from the baseline injection velocity, the average soot concentration changes moderately. This trend can be partly explained by the fuel residence time. As the fuel injection velocity decreases, the fuel particles stay longer in the combustion zone, leading to a higher soot concentration.

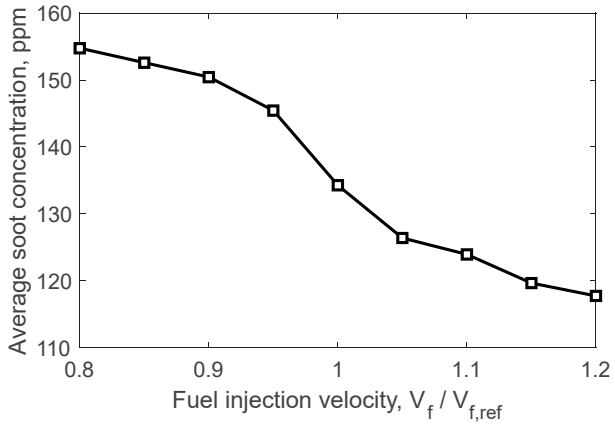

Figure 19. Effect of the fuel injection velocity on the soot concentration.

Therefore, it can be observed that the fuel injection velocity is a promising control parameter. For a slightly higher fuel injection velocity, the combustor efficiency remains almost the same, while soot emissions reduced significantly. The finding suggests that a relatively high injection velocity fuel injector design concept can potentially reduce soot emissions.

5. Conclusions and Future Works

The current study explored the aerothermal performance and emission characteristics of a micro-gas turbine combustor, with a focus on its potential use in radio-controlled unmanned aerial vehicles. There are few works available in the public domain that attempt to model simultaneously the aerothermal performance and emissions of a micro-gas turbine. A comprehensive CFD model was developed in the work to model the reacting flow in the combustion chamber. The numerical model of the whole engine was validated against the experimental data and the throughflow model at the maximum thrust condition, which is also the operating point investigated in the current work.

Based on the numerical results and analyses presented in the current work, it can be concluded that the aerothermal performance and emission characteristics of the micro-gas turbine combustor are strongly influenced by various parameters. The main points are summarized below:

1. Non-uniform outlet pressure can occur at the combustor–turbine interface due to the potential field of downstream nozzle guide vanes. It increases the maximum temperature at the hot spot. Combustor efficiency slightly decreases, and soot emissions significantly increase for the simulation with non-uniform outlet pressure boundary condition. The findings suggest that a two-dimensional boundary condition is required for the combustor simulation instead of an average value obtained from the cycle analysis for an improved prediction. The uniform outlet boundary condition simulation overestimates the calculation of the combustion efficiency and underestimates the soot emissions prediction.
2. A lower fuel-to-air ratio results in a higher combustion efficiency. The fuel-to-air ratio has a significant impact on the hot-spot temperature level and location, with an increase in maximum temperature as the fuel-to-air ratio increases. The fuel-to-air

ratio has a non-monotonic effect on the soot emissions. The optimum value is around 1.05 times the baseline value. Any fuel-to-air ratio smaller or larger than the optimum value results in higher soot emissions.

3. The fuel injection velocity has insignificant impact on both the combustion efficiency and the hot-spot level and location. The fuel injection velocity has a monotonic but non-linear relationship with soot emissions. As the fuel injection velocity decreases, soot emissions consistently increase.

The findings of the current paper provide valuable information for improving the performance and emission characteristics of micro-gas turbine combustors. In the next steps, the interaction between the combustor and the turbine is further analyzed in more detail, based on the promising results preliminarily obtained in the current work. To meet the objectives of the project, potential modifications of the existing micro-gas turbine design shall be explored to mitigate the adverse effects.

Author Contributions: Conceptualization, H.W. and K.H.L.; methodology, H.W.; software, H.W.; validation, H.W.; formal analysis, H.W. and K.H.L.; investigation, H.W. and K.H.L.; data curation, H.W.; writing—original draft preparation, H.W.; writing—review and editing, H.W. and K.H.L.; visualization, H.W.; supervision, K.H.L. All authors have read and agreed to the published version of the manuscript.

Funding: ARCHER2 supercomputing resources provided by the UK Engineering and Physical Sciences Research Council under the project "UK Consortium on Mesoscale Engineering Sciences (UKCOMES)" (Grant No. EP/X035875/1) are gratefully acknowledged. This work made use of computational support by CoSeC, the Computational Science Centre for Research Communities, through UKCOMES.

Data Availability Statement: Not applicable.

Conflicts of Interest: The authors declare no conflict of interest.

References

1. De Robbio, R. Micro gas turbine role in distributed generation with renewable energy sources. *Energies* **2023**, *16*, 704. [CrossRef]
2. Banihabib, R.; Assadi, M. The role of micro gas turbines in energy transition. *Energies* **2022**, *15*, 8084. [CrossRef]
3. Ji, F.; Zhang, X.; Du, F.; Ding, S.; Zhao, Y.; Xu, Z.; Wang, Y.; Zhou, Y. Experimental and numerical investigation on micro gas turbine as a range extender for electric vehicle. *Appl. Therm. Eng.* **2020**, *173*, 115236. [CrossRef]
4. Capata, R.; Saracchini, M. Experimental campaign tests on ultra micro gas turbines, fuel supply comparison and optimization. *Energies* **2018**, *11*, 799. [CrossRef]
5. Habib, Z.; Parthasarathy, R.; Gollahalli, S. Performance and emission characteristics of biofuel in a small-scale gas turbine. *Appl. Energy* **2013**, *87*, 1701–1709. [CrossRef]
6. Large, J.; Pesyiridis, A. Investigation of micro gas turbine systems for high speed long loiter tactical unmanned air systems. *Aerospace* **2019**, *6*, 55. [CrossRef]
7. Okafor, E.C.; Somarathne, K.K.A.; Hayakawa, A.; Kudo, T.; Kurata, O.; Iki, N.; Kobayashi, H. Towards the development of an efficient low-NOx ammonia combustor for a micro gas turbine. *Proc. Combust. Inst.* **2019**, *37*, 4597–4606. [CrossRef]
8. Zong, C.; Ji, C.; Cheng, J.; Zhu, T.; Guo, D.; Li, C.; Duan, F. Toward off-design loads: Investigations on combustion and emissions characteristics of a micro gas turbine combustor by external combustion-air adjustments. *Energy* **2022**, *253*, 124194. [CrossRef]
9. Lefebvre, A.H. Fuel effects on gas turbine combustion-liner temperature, pattern factor, and pollutant emissions. *J. Aircr.* **1984**, *21*, 887–898. [CrossRef]
10. Chmielewski, M.; Niszczota, P.; Gieras, M. Combustion efficiency of fuel-water emulsion in a small gas turbine. *Energy* **2020**, *211*, 118961. [CrossRef]
11. Chmielewski, M.; Gieras, M. Impact of variable geometry combustor on performance and emissions from miniature gas turbine engine. *J. Energy Inst.* **2017**, *90*, 257–264. [CrossRef]
12. Naegeli, D.W.; Dodge, L.G.; Moses, C.A. Effects of flame temperature and fuel composition on soot formation in gas turbine combustors. *Combust. Sci. Technol.* **1983**, *35*, 117–131. [CrossRef]
13. Rault, T.M.; Vishwanath, R.B.; Gülder, Ö.L. Impact of ethanol blending on soot in turbulent swirl-stabilized Jet A-1 spray flames in a model gas turbine combustor. *Proc. Combust. Inst.* **2021**, *38*, 6431–6439. [CrossRef]
14. Wang, H.; Luo, K.H. Numerical investigation of dump diffuser combustor performance at uniform and non-uniform inlet conditions. In Proceedings of the Turbo Expo: Power for Land, Sea, and Air, London, UK, 21–25 September 2020; GT2020-15982. [CrossRef]

15. Denton, J.D. Some limitations of turbomachinery CFD. In Proceedings of the Turbo Expo 2010: Power for Land, Sea, and Air, Glasgow, UK, 14–18 June 2010; Volume 7, pp. 735–745, GT2010-22540. [CrossRef]
16. Wagner, J.H.; Dring, R.P.; Joslyn, H.D. Inlet boundary layer effects in an axial compressor rotor: Part I—Blade-to-blade effects. *J. Eng. Gas Turbine Power* **1985**, *107*, 374–380. [CrossRef]
17. Phan, H.M.; He, L. Validation studies of linear oscillating compressor cascade and use of influence coefficient method. *J. Turbomach.* **2020**, *142*, 051005. [CrossRef]
18. Phan, H.M.; He, L. Efficient steady and unsteady flow modeling for arbitrarily mis-staggered bladerow under influence of inlet distortion. *J. Eng. Gas Turbine Power* **2021**, *143*, 071009. [CrossRef]
19. Phan, H.M. Modeling of a turbine bladerow with stagger angle variation using the multi-fidelity influence superposition method. *Aerosp. Sci. Technol.* **2022**, *121*, 107318. [CrossRef]
20. Phan, H.M.; He, L. Efficient modeling of mistuned blade aeroelasticity using fully-coupled two-scale method. *J. Fluids Struct.* **2022**, *115*, 103777. [CrossRef]
21. Cha, C.M.; Hong, S.; Ireland, P.T.; Denman, P.; Savarianandam, V. Experimental and numerical investigation of combustor-turbine interaction using an isothermal, nonreacting tracer. *J. Eng. Gas Turbine Power* **2012**, *134*, 081501. [CrossRef]
22. Miki, K.; Moder, J.; Liou, M.S. Computational study of combustor-turbine interactions. *J. Propuls. Power* **2018**, *34*, 1529–1541. [CrossRef]
23. Phan, H.M.; Duan, P.H.; Dinh, C.T. Numerical aero-thermal study of high-pressure turbine nozzle guide vane: Effects of inflow conditions. *Phys. Fluids* **2020**, *32*, 034111. [CrossRef]
24. Shang, T.; Epstein, A.H. Analysis of hot streak effects on turbine rotor heat load. *J. Turbomach.* **1997**, *119*, 544–553. [CrossRef]
25. Dorney, D.J.; Davis, R.L.; Edwards, D.E.; Madavan, N.K. Unsteady analysis of hot streak migration in a turbine stage. *J. Propuls. Power* **1992**, *8*, 520–529. [CrossRef]
26. Barth, T.; Jespersen, D. The design and application of upwind schemes on unstructured meshes. In Proceedings of the 27th Aerospace Sciences Meeting, Reno, NV, USA, 9–12 January 1989. AIAA 89-0366. [CrossRef]
27. Rhie, C.M.; Chow, W.L. Numerical study of the turbulent flow past an airfoil with trailing edge separation. *AIAA J.* **1983**, *21*, 1525–1532. [CrossRef]
28. Menter, F.R. Two-equation eddy-viscosity turbulence models for engineering applications. *AIAA J.* **1994**, *32*, 1598–1605. [CrossRef]
29. Lee, C.M.; Kundu, K.; Ghorashi, B. Simplified jet-A kinetic mechanism for combustor application. In Proceedings of the 31st Aerospace Sciences Meeting, Reno, NV, USA, 11–14 January 1993. AIAA-93-0021. [CrossRef]
30. Cameretti, M.C.; Piazzesi, R.; Reale, F.; Tuccillo, R. Comparison of external and internal EGR concepts for low emission micro gas turbines. In Proceedings of the ASME Turbo Expo 2012: Power for Land, Sea, and Air, Glasgow, UK, 14–18 June 2010; Volume 3, pp. 581–593, GT2010-22413. [CrossRef]
31. Camaretti, M.C.; Tuccillo, R.; Piazzesi, R. Study of an exhaust gas recirculation equipped micro gas turbine supplied with bio-fuels. *Appl. Therm. Eng.* **2013**, *59*, 162–173. [CrossRef]
32. Xing, C.; Liu, L.; Qiu, P.; Shen, W.; Lyu, Y.; Zhang, Z.; Wang, H.; Wu, S.; Qin, Y. Combustion performance of an adjustable fuel feeding combustor under off-design conditions for a micro-gas turbine. *Appl. Energy* **2017**, *208*, 12–24. [CrossRef]
33. O'Rourke, P.J.; Amsden, A.A. The TAB method for numerical calculation of spray droplet breakup. In Proceedings of the International Fuels and Lubricants Meeting and Exposition, Toronto, ON, Canada, 2 November 1987; LA-UR-87-2105-Rev. [CrossRef]
34. Tanner, F.X. Liquid jet atomization and droplet breakup modeling of non-evaporating diesel fuel sprays. *SAE Trans.* **1997**, *106*, 127–140. [CrossRef]
35. Tanner, F.X. Development and validation of a cascade atomization and drop breakup model for high-velocity dense sprays. *At. Sprays* **2004**, *14*, 32. [CrossRef]
36. Reitz, R.D.; Diwakar, R. Structure of high-pressure fuel sprays. *SAE Trans.* **1987**, *96*, 492–509. [CrossRef]
37. Wahba, E.M.; Nawar, H. Multiphase Flow Modeling and optimization for online wash systems of gas turbines. *Appl. Math. Model.* **2013**, *37*, 7549–7560. [CrossRef]
38. Sedarsky, D.; Paciaroni, M.; Berrocal, E.; Petterson, P.; Zelina, J.; Gord, J.; Linne, M. Model validation image data for breakup of a liquid jet in crossflow: Part I. *Exp. Fluids* **2010**, *49*, 391–408. [CrossRef]
39. Liu, H.F.; Li, W.F.; Gong, X.; Cao, X.K.; Xu, J.L.; Chen, X.L.; Wang, Y.F.; Yu, G.S.; Wang, F.C.; Yu, Z.H. Effect of liquid jet diameter on performance of coaxial two-fluid airblast atomizers. *Chem. Eng. Process.* **2006**, *45*, 240–245. [CrossRef]
40. Magnussen, B.F.; Hjertager, B.H. On mathematical modeling of turbulent combustion with special emphasis on soot formation and combustion. *Symp. (Int.) Combust.* **1977**, *16*, 719–729. [CrossRef]
41. Tesner, P.A.; Smegiriova, T.D.; Knorre, V.G. Kinetics of dispersed carbon formation. *Combust. Flame* **1971**, *17*, 253–260. [CrossRef]
42. Schreckling, K. *Home Built Model Turbines*; Traplet Publications Limited: Worcestershire, UK, 2005.
43. Teixera, M.; Romagnosi, L.; Mezine, M.; Baux, Y.; Anker, J.; Claramunt, K.; Hirsch, C. A methodology for fully-coupled CFD engine simulations, applied to a micro gas turbine engine. In Proceedings of the Turbo Expo 2018: Power for Land, Sea, and Air, Oslo, Norway, 11–15 June 2018; Volume 2C, GT2018-76870. [CrossRef]
44. Yang, C.; Wu, H.; Du, J.; Zhang, H.; Yang, J. Full-engine simulation of micro gas turbine based on time-marching throughflow method. *Appl. Therm. Eng.* **2022**, *217*, 119213. [CrossRef]

45. Xiang, J.; Schlüter, J.U.; Duan, F. Study of KJ-66 micro gas turbine compressor: Steady and unsteady Reynolds-averaged Navier-Stokes approach. *Proc. Inst. Mech. Eng. Part G: J. Aerosp. Eng.* **2017**, *231*, 904–917. [CrossRef]
46. Briones, A.M.; Caswell, A.W.; Rankin, B.A. Fully coupled turbojet engine computational fluid dynamics simulations and cycle analyses along the equilibrium running line. *J. Eng. Gas Turbines Power* **2021**, *143*, 061019. [CrossRef]
47. He, Y.; Kim, C.H. Effect of nozzle port shape of fuel injector of micro gas turbine engine combustor on mixture gas formation for combustion. *Fluids* **2022**, *7*, 184. [CrossRef]